ACS Catalysis

Open Access

pubs.acs.org/acscatalysis

Research Article

Free-Energy Landscapes and Surface Dynamics in Methane Activation on Ni(511) via Machine Learning and Enhanced Sampling

Yezhi Jin,[#] Yinan Xu,*[,#] Jireh S. García Sánchez, Gustavo R. Pérez-Lemus, Pablo F. Zubieta Rico, Massimiliano Delferro, and Juan J. de Pablo*

Cite This: *ACS Catal.* 2025, 15, 8931−8942

Read Online

ACCESS | Metrics & More | Article Recommendations | Supporting Information

ABSTRACT: Methane activation on stepped Ni(511) surfaces involves the rearrangement of surface atoms as the chemical reaction proceeds. This process is particularly sensitive to temperature. Using machine-learned interatomic potentials (MLIPs) coupled with enhanced sampling techniques, we investigate the activation of methane under realistic operando conditions. Our analysis reveals that methane dissociation occurs predominantly at step-edge nickel atoms. As CH_x (where x = 3 or 4) species bind to additional surface nickel atoms, their reduced mobility leads to entropic penalties that suppress certain configurations and transition states. This is reflected in the underlying free energy surfaces, where configurations such as methyl binding to hollow sites and activation routes involving two nickel atoms become unfavorable as temperature increases. At elevated temperatures, methane activation extends from step-edge sites to terrace regions because of reduced free-energy barriers and enhanced surface dynamics. By decomposing the free-energy into enthalpic and entropic contributions, we uncover temperature-dependent shifts in the preferences of methane for the relevant active sites and arrive at a detailed molecular picture of methane activation.

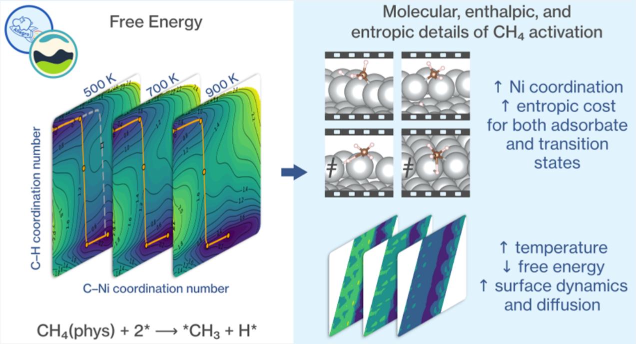

KEYWORDS: *methane activation, surface defects, machine-learned interatomic potentials, dynamic sampling, transition metal catalysts, entropy effects in catalysis*

1. INTRODUCTION

The conversion of methane into value-added chemicals provides an opportunity to mitigate its impact as a greenhouse gas, while addressing the growing demand for industrial feedstocks.[1−7] Extensive research efforts have focused primarily on the direct synthesis of methanol from methane[8−15] and the production of syngas through methane steam or dry reforming in heterogeneous catalytic systems.[16−23] In both direct oxidation of methane and methane reforming, the conversion of methane to high value chemicals and fuels remains a significant challenge due to the high dissociation energy of the first C−H bond in methane (~440 kJ mol^{-1}), which requires extreme operando conditions, typically involving elevated temperatures (800−1100 K), to promote bond cleavage.[18,24−29] Notably, the initial C−H bond breaking step is often rate-limiting and governs the overall reaction rates in various methane chemistries.[30−37] Therefore, the development of efficient catalysts for methane conversion and relatively facile methane activation requires that advanced characterization techniques and detailed computational methods at the atomic level, capable of generating new knowledge under operando conditions.

From a computational perspective, static density functional theory (DFT) calculations have been widely employed to elucidate the nature of active sites, reaction intermediates, and the energetics of the overall reaction mechanism on a variety of pristine and modified metal surfaces.[9,24,30,31,35,38−40] However, efficient and accurate descriptions of the dynamic nature of the catalyst surface at realistic operating conditions are beyond the reach of the static DFT approach. *Ab initio* molecular dynamics (AIMD) simulations can incorporate finite-temperature effects and capture surface dynamics.[41−44] However, the high computational cost of AIMD often limits such calculations to short time scales and small systems, resulting in insufficient sampling of high-energy states and rare events critical to methane activation.

Recent advances in machine-learned interatomic potentials (MLIPs) coupled with flexible, enhanced sampling methods

Received: January 27, 2025
Revised: April 24, 2025
Accepted: April 28, 2025

https://doi.org/10.1021/acscatal.5c00724

have emerged as a powerful tool to conduct reactive molecular dynamics (MD) simulations that narrow the computational efficiency gap at realistic operating conditions. By learning the force and energy produced from *ab initio* simulations, machine learning models such as neural networks can serve as an interatomic potential that maintains high accuracy at a fraction of the computational cost of AIMD.[45−56] Compared to traditional methods, MLIPs exhibit minimal deviations from *ab initio* reference calculations, with force errors typically below 0.1 eV/Å, while achieving significant speedups, particularly when implemented on GPU-accelerated platforms. These capabilities have been demonstrated in studies of N_2 decomposition on Fe(111),[57,58] ammonia cracking on Fe(110) and Fe(111),[59] and methane activation on Ni(111).[60] These successes have thus far been limited to idealized, low-index metal surfaces, which fail to capture the full complexity of industrial catalysts under operando conditions. Important dynamic phenomena such as active site evolution, variations in surface reactivity, and the complex, temperature-dependent free-energy landscapes that emerge during realistic catalytic processes remain to be explored.

In this study, we present a workflow that combines MLIPs with enhanced sampling techniques to investigate the temperature-dependent activation of a physisorbed methane molecule on a Ni(511) surface under realistic operando conditions, represented by the following reaction: $CH_4(phys) + 2^* \rightarrow {}^*CH_3 + H^*$, where * denotes an active site on the Ni(511) surface. Specifically, we rely on MD simulations using a purposely developed MLIP, combined with Spectral Adaptive Biasing Force (Spectral ABF) sampling,[61] to construct the free energy surface that governs methane activation, and elucidate the entropic and enthalpic contributions to this process on the underlying stepped nickel surfaces at 500−1100 K. By highlighting temperature-induced shifts in transition states, adsorption modes, and reaction coordinates, our findings provide new mechanistic insights of general interest to the catalysis community and establish a framework for exploring entropically driven phenomena on defected surfaces.

As depicted in Figure 1, the Ni(511) surface features a diverse set of atomic environments.[30,32] In our simulations, methane interacts dynamically with these surface sites, generating temperature-dependent free-energy landscapes. We observe that methane initially coordinates to step-edge nickel atoms before any C−H bond cleavage, leading to a modest enthalpic rise but a significant entropic penalty from restricted molecular mobility. Upon crossing the transition state, the adsorbed species regain some mobility, resulting in a significant increase in entropy. When CH_x ($x = 3$ or 4) binds to multiple nickel atoms, such as at bridge or hollow sites, its mobility decreases further and its entropy decreases accordingly, particularly at elevated temperatures where certain configurations vanish from the free-energy surfaces. Furthermore, our results show that methane activation is not limited to step edges at high temperatures; terrace sites also become active driven by both nickel−methane interactions and thermal fluctuations. In general, we reveal how the temperature reshapes the free energy landscape of methane activation in surprising ways, and we underscore the adaptive, dynamic nature of catalytic sites under realistic conditions.

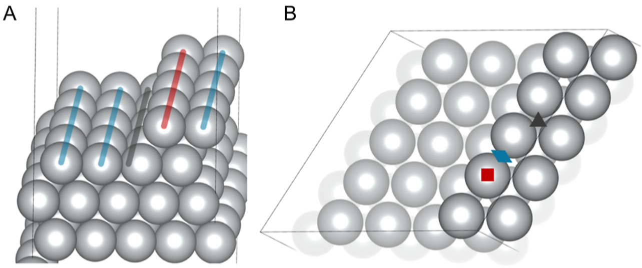

Figure 1. (A) Side view of the Ni(511) surface with nickel atom rows colored red, blue, and gray, representing step sites (SS), terrace sites (TS), and other sites (OS), respectively. (B) Top view of the Ni(511) surface showing step-atop, step-bridge, and fcc-hollow sites marked as square, diamond, and triangle, respectively.

2. RESULTS AND DISCUSSION

2.1. Molecular and Thermodynamic Details of Methane Activation on Ni(511). To investigate the thermodynamic and molecular details of the activation of a physisorbed methane molecule on the Ni(511) surface, we computed the two-dimensional (2D) free energy surfaces (FES's) at 500, 700, 900, and 1100 K using MLIP molecular dynamics (MLIP-MD) with enhanced sampling. The FES's, shown in Figure 2A−C, are constructed using two collective variables (CVs): the C−Ni coordination number (CN_{C-Ni}), which quantifies the interaction between methane and the Ni surface, and CN_{C-H}, which describes the dissociation state of one arbitrary C−H bond of methane. We determine the minimum free energy path (MFEP) using the AutoNEB algorithm[62] with the climbing image scheme[63] over the FES and identify critical states along the path. We refer to the resulting path as MFEP1. In this section, we provide a detailed examination of the FES and MFEP1 at 700 K, highlighting the key molecular interactions and thermodynamic features associated with methane activation on the Ni(511) surface.

As shown in Figure 2A−C, the FES exhibits two main local minima. The first minimum, denoted as state 0 and located at the CV values of (0.02, 3.87), corresponds to the initial state. Here, the carbon atom is not coordinated with any nickel atoms, and the physisorbed methane molecule remains intact and is reasonably distant from the nickel surface. The second local minimum, denoted as state 4 and located at (1.90, 2.90), represents the product state. In this state, a hydrogen atom has been liberated onto the surface, leaving an adsorbed methyl molecule that occupies a bridge site. This is indicated by the CN_{C-Ni} of 1.90 showing that the carbon atom in the methyl group binds, on average, to two surface nickel atoms. Along the MFEP1 that connects the local minima, the activation process proceeds through distinct molecular and energetic changes, divided into four segments: from states 0 to 1, 1 to 2, 2 to 3, and 3 to 4.

The first segment extending from state 0 to 1, corresponds to a gradual increase in CN_{C-Ni} from 0.02 to 0.92, while CN_{C-H} remains nearly constant around 3.85, indicating that no C−H bond cleavage has occurred yet. Representative molecular configurations corresponding to each state are shown in Figure 2D, illustrating that the methane molecule approaches the nickel surface without significant activation of any C−H bond. This process marks a gradual increase in free energy, which can be separated into the enthalpic (ΔH) and entropic ($-T\Delta S$) contributions, as shown in Figure 2E−G. At 700 K, the enthalpy increases slightly by 0.15 eV, which is attributed to the increased repulsion between the approaching methane molecule and the nickel surface, without any C−H

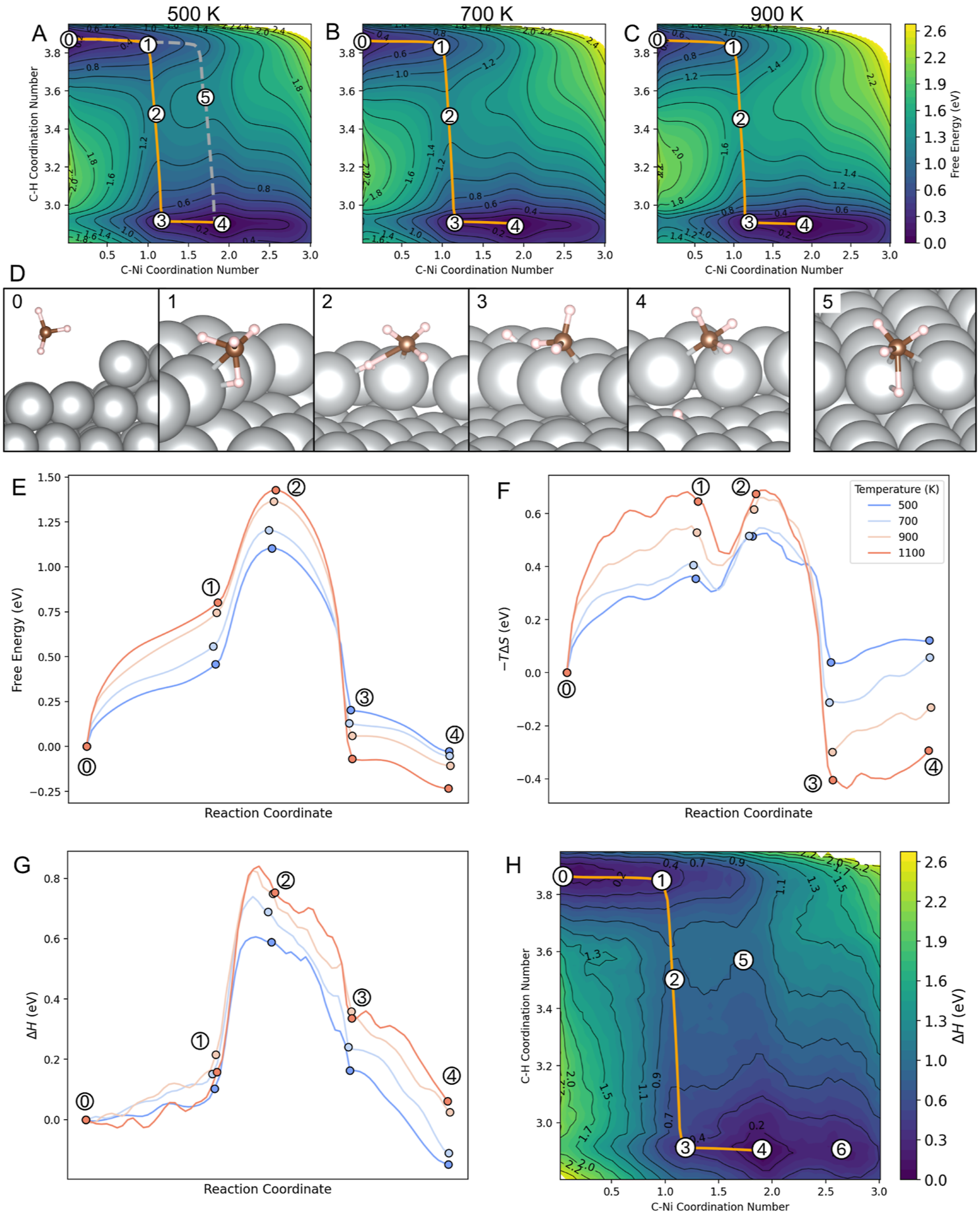

Figure 2. (A−C) Free energy diagram for methane activation based on MLIP-MD with Spectral-ABF sampling scheme, with the MFEP1 and MFEP2 highlighted in orange and gray, respectively, at 500, 700, and 900 K. (D) Representative molecular schematics of the key states along the MFEPs (Ni = gray, C = brown, and H = white). (E−G) Details of the MFEP1 and the key states in terms of free energy, enthalpy, and the "$-TS$" entropic contribution. (H) 2D enthalpic contribution profile based on the MLIP-MD at 700 K. The free energy analysis in E−G treats the physisorbed methane as the reference state, which is zero for all temperatures.

bond cleavage occurring. Meanwhile, there is a significant increase in the $-T\Delta S$ term, 0.41 eV at 700 K, indicating a decrease in the entropy of the system. We attribute this entropy change to the strong methane-surface interactions at the step edge. In state 0, the methane molecule retains some motion along the z direction (perpendicular to the surface). In state 1, this vertical motion is restricted due to increased interactions of the molecule with the nickel surface. More importantly, at state 1, both the hydrogen and carbon atoms of methane interact with a surface nickel atom, with mean Ni−H and Ni−C distances of 1.7 and 2.2 Å, respectively (Figure 2D1). This interaction is distinctive to the step-edge nickel atoms because of their under-coordinated nature and higher reactivity compared to the terrace nickel atoms. On Ni(111), we observe only subtle Ni−H interactions at state 1.[60] On Ni(511), the presence of both Ni−H and Ni−C interactions for the step-edge Ni atoms at state 1 imposes significant constraints on the mobility of the methane molecule in the x−y plane. These restrictions on the translation and rotation of methane contribute to the observed decrease in entropy.

In the second segment of MFEP1 (states 1 to 2), the system approaches the transition state that leads to the dissociation of a C−H bond. This segment is characterized by a notable decrease in CN_{C-H} (3.49 at state 2) and a slight increase in CN_{C-Ni} (1.07 at state 2). In the transition state (state 2), there is a more pronounced elongation of the C−H bond oriented toward one nickel atom at the step edge, where the mean C−H distance increases to 1.7 Å at 700 K. As seen in Figure 2D3, the nickel atom binds to both carbon and hydrogen atoms, where the mean Ni−C and Ni−H distances are 2.0 and 1.5 Å respectively. Meanwhile, the hydrogen atom of the activated C−H bond weakly interacts with an adjacent nickel atom with a mean distance of 1.7 Å at 700 K. We note that some bonding features in state 2 are similar to those in state 1, where the nickel atom interacts with both the carbon and hydrogen atoms of methane. The main difference is the further stretching of the C−H bond in state 2. Therefore, the constraints on the mobility of methane molecule remain similar between states 1 and 2, and the entropy of the system decreases only slightly during this segment, leading to a minor increase in the $-T\Delta S$ term of 0.11 eV at 700 K (Figure 2F). The slight decrease in entropy may also be attributed to the participation of an additional nickel atom in the transition state, which adds additional constraints on the molecule's motion. Notably, a slight "dip" in the $-T\Delta S$ profile between states 1 and 2 is consistent with our earlier observations on Ni(111),[60] where C−H and Ni−H pairs form and break intermittently, leading to the translational and rotational freedom of methane before the transition state. Although the effect here is less pronounced, we attribute the small local minimum in the $-T\Delta S$ curve on Ni(511) to the same molecular behavior: transient increases in methane mobility arising from these dynamic bond switching interactions at the step edge. On the other hand, the enthalpy of the system increases sharply throughout this segment, reaching 0.69 eV, because of the significant energy required to elongate and partially break the strong C−H bond while the carbon and hydrogen atoms remain bonded (Figure 2G). This sharp enthalpic increase contributes significantly to the pronounced increase in free energy observed in the second segment of the MFEP1. The combined effect of the increase in enthalpy and the slight entropic contribution leads to the peak of the MFEP1 at the transition state (Figure 2E).

The third segment of MFEP1 extends from the transition state (state 2) to a local minimum (state 3), marking the complete cleavage of the C−H bond in methane and the formation of a methyl group ($*CH_3$) and an adsorbed hydrogen atom (*H). In this segment, the CN_{C-H} decreases significantly from approximately 3.49 at state 2 to 2.91 at state 3 at 700 K, indicating that a hydrogen atom has fully dissociated from the carbon atom. The methyl group stabilizes on the Ni(511) surface. As reflected in Figure 2D4, the methyl group preferentially binds to a nickel step atom in the atop geometry. The carbon atom forms a strong bond with a single nickel atom at the step edge, with a mean Ni−C bond distance of 2.04 Å at 700 K. Furthermore, the carbon atom weakly interacts with an adjacent nickel atom, resulting in an effective Ni−C CN of 1.17 (Figure 2B). The enthalpy profile (Figure 2H) shows a pronounced drop after the transition state, corresponding to the formation of the full Ni−C and Ni−H bonds. In addition, the system experiences a notable increase in entropy during this segment, as indicated by a decrease in the $-T\Delta S$ term of 0.63 eV at 700 K (Figure 2F). The methyl group, now adsorbed on the surface, is no longer constrained by the geometrical limitations observed in the transition state. The surface-bound methyl group acquires more rotational and translational freedom on the surface, particularly along the step edge. The adsorbed hydrogen atom, capable of diffusing across the surface, also contributes to the increase in entropy. The combined effect of a sharp enthalpy decrease and a pronounced entropy increase results in a significant reduction in the free energy of the system in this segment of the MFEP1 (Figure 2E).

In the final segment of the MFEP1, the adsorbed methyl group migrates from an atop site, where it binds to a single nickel atom, to a bridge site, where it binds to two nickel atoms. This migration results in an increase in the C−Ni coordination number from 1.17 to 1.90, while the C−H coordination number remains nearly constant at 2.90 in state 4 at 700 K (Figure 2B). The move of the methyl group to the bridge site leads to a stronger and more favorable binding to the nickel surface, evidenced by a continuing decrease in the enthalpy of the system in Figure 2H. Figure 2D5 indicates that the methyl group bridges two nickel atoms at the step edge, with mean Ni−C bond distances of 2.0 Å at 700 K. However, this final segment shows a slight decrease in entropy, reflected by a minor increase in the $-T\Delta S$ term (0.16 eV at 700 K). The entropy change suggests that as the methyl group migrates from an atop to the bridge site, its mobility slightly decreases. Nevertheless, the substantial decrease in enthalpy outweighs the minor entropic change, resulting in an overall decrease in free energy of the system (−0.18 eV at 700 K).

Figure 2E illustrates how temperature (ranging from 500 to 1100 K) impacts the relative height of the MFEP1 on the Ni(511) surface. The physisorbed methane molecule is treated as the reference state with zero free energy at all temperatures. However, we note that if the gas-phase methane was chosen as the reference, the free-energy barriers would become even more sensitive to temperature because of the additional entropy loss upon adsorption, thus magnifying the observed trends.

Our results reveal that the activation free energy barrier along the MFEP1 increases with temperature. This trend indicates that as the system progresses from the reactant to the transition state, the activation process is associated with an overall reduction in the mobility of the methane molecule, particularly due to the loss of mobility along the z-direction (perpendicular to the surface) compared to the initial physisorbed state (states 0−1).

When we examine the trend of the reaction free energy, we find that, unlike the activation energy barrier, it decreases with increasing temperature. This opposite trend suggests that the overall thermodynamics of the reaction become more favorable at higher temperatures. The decrease in reaction free energy is largely driven by the reaction entropy. We focus on the reaction entropy, which corresponds to the difference in the $-T\Delta S$ term between the reactant (initial physisorbed methane) and the product (adsorbed methyl group and hydrogen atom) state. At lower temperatures (500 to 700 K), the reaction entropy is nearly zero, indicating that the difference in entropy between the reactant and product is minimal. However, at higher temperatures (900 and 1100 K), the $-T\Delta S$ term becomes increasingly negative, suggesting a significant increase in entropy in the final adsorbed state compared to the initial physisorbed state. This trend is particularly evident in the segment of the entropy profile from the transition state to the final adsorbed state, where the $-T\Delta S$ term decreases sharply at higher temperatures, indicating that

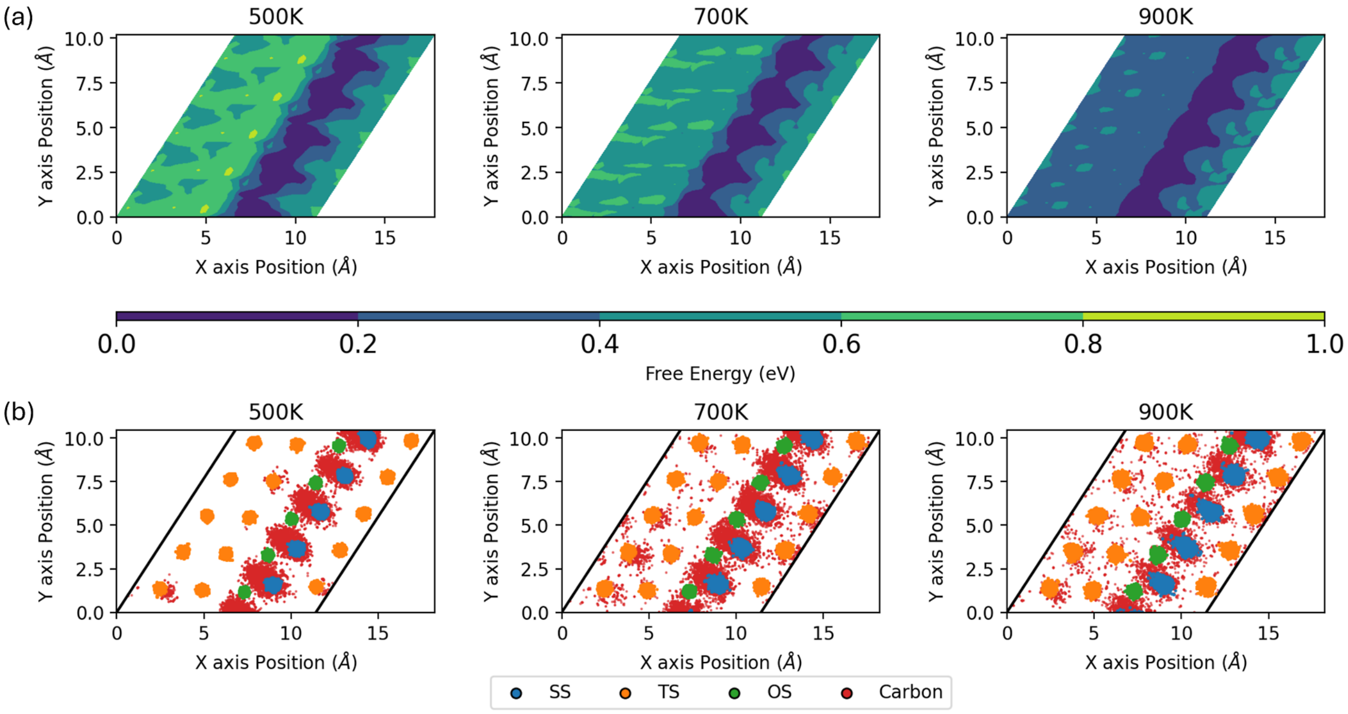

Figure 3. (a) Free energy surfaces (FES) reconstructed using posthoc Spectral-ABF analysis at temperatures of 500, 700, and 900 K. Additional postprocessing was applied to enforce cyclic symmetry on the FES. Detailed methodology is provided in the Methods section. (b) Statistical distribution of carbon and nickel atom positions at the transition state (state 2) along the minimum free energy path 1 (MFEP1).

the system gains entropy by forming the adsorbed methyl group and hydrogen atom at elevated temperatures. This behavior is consistent with our previous analysis of methane activation on the Ni(111) surface,[60] where we observed a similar trend and attributed the increase in entropy at higher temperatures to the role of surface atom vibrations that facilitate the mobility of the adsorbed methyl group. Here on Ni(511), these intensified phonon-driven vibrations work in tandem with enhanced mobility of the product species (CH_3 and H), where the probability of adsorbate migrating from one site to another increases markedly with temperature, indicating that a higher thermal energy not only propels the adsorbates more intensely but also allows them to overcome diffusion barriers between adsorption sites. This collective effect further increases the mobility of the adsorbed methyl group and hydrogen atom, contributing to the entropic gains and the more exergonic nature of methane dissociation at elevated temperatures. In addition, we computed the subsequent C−H bond cleavage of adsorbed $^*CH_3$ to form $^*CH_2$ + *H at 900 K using a MLIP trained via the same workflow (see Methods and Supporting Information). The activation free energy for this step is approximately 0.60 eV, significantly lower than that of the initial C−H bond cleavage in methane, suggesting that the first C−H bond dissociation of CH_4 is the most likely rate-determining step among the sequential bond-breaking processes.

2.2. Temperature Effects on the Nature, Dynamics, and Thermodynamic Favorability of Active Sites. The analysis of the enthalpic contributions to the FES at 700 K, shown in Figure 2H, reveals an additional local minimum, referred to as state 6, where the C−H and C−Ni coordination numbers are 2.62 and 2.91, respectively. This state represents a methyl molecule binding to a hollow site on the Ni(511) surface. Our analysis of the molecular configurations at state 6 reveals that these hollow sites consist primarily of nickel atoms at the step edge and additional nickel atoms located on the terrace portion of the Ni(511) surface. Although state 6 is distinguishable as a local minimum in the enthalpy profile at 700 K, it does not appear in the overall FES at this temperature (Figure 2B). Notably, state 6, though present in the enthalpic profiles, is absent in FES's at all temperatures considered here (500, 700, 900, and 1100 K). We attribute this behavior to entropic effects, similar to the entropy difference observed between the atop site and the bridge site configurations (states 3−4 in Figure 2F). As the methyl moiety binds to more surface nickel atoms, transitioning from atop to bridge to hollow sites, its mobility decreases due to increased bonding constraints. Such a trend makes the configuration increasingly entropically unfavorable at higher temperatures, which explains the absence of state 6 in the FES's.

This entropic trend is not limited to the methyl group but also applies to the $[H{-}CH_3]^{\ddagger}$ transition state. In addition to the MFEP1, a second methane activation route, referred to as MFEP2, can be identified on the FES at 500 K, as well as the enthalpic contribution profile in Figure 2H. As shown in Figure 2A, starting from state 0, MFEP2 extends to a CV location with a higher value of the C−Ni coordination number compared to the MFEP1. At 500 K, the transition state along the MFEP2 has CV values of 1.71 for the CN_{C-Ni} and 3.57 for CN_{C-H}, suggesting that during methane activation, the carbon atom binds simultaneously to two nickel atoms. Analysis of the MD frames at the transition state reveals that this activation route involves one stretched C−H bond, with the carbon atom interacting with two adjacent nickel atoms on the step edge of the Ni(511) surface (Figure 2D5). After the C−H bond cleavage, the methyl group is directly stabilized by coordination with the two nickel atoms at the bridge site (state 4).

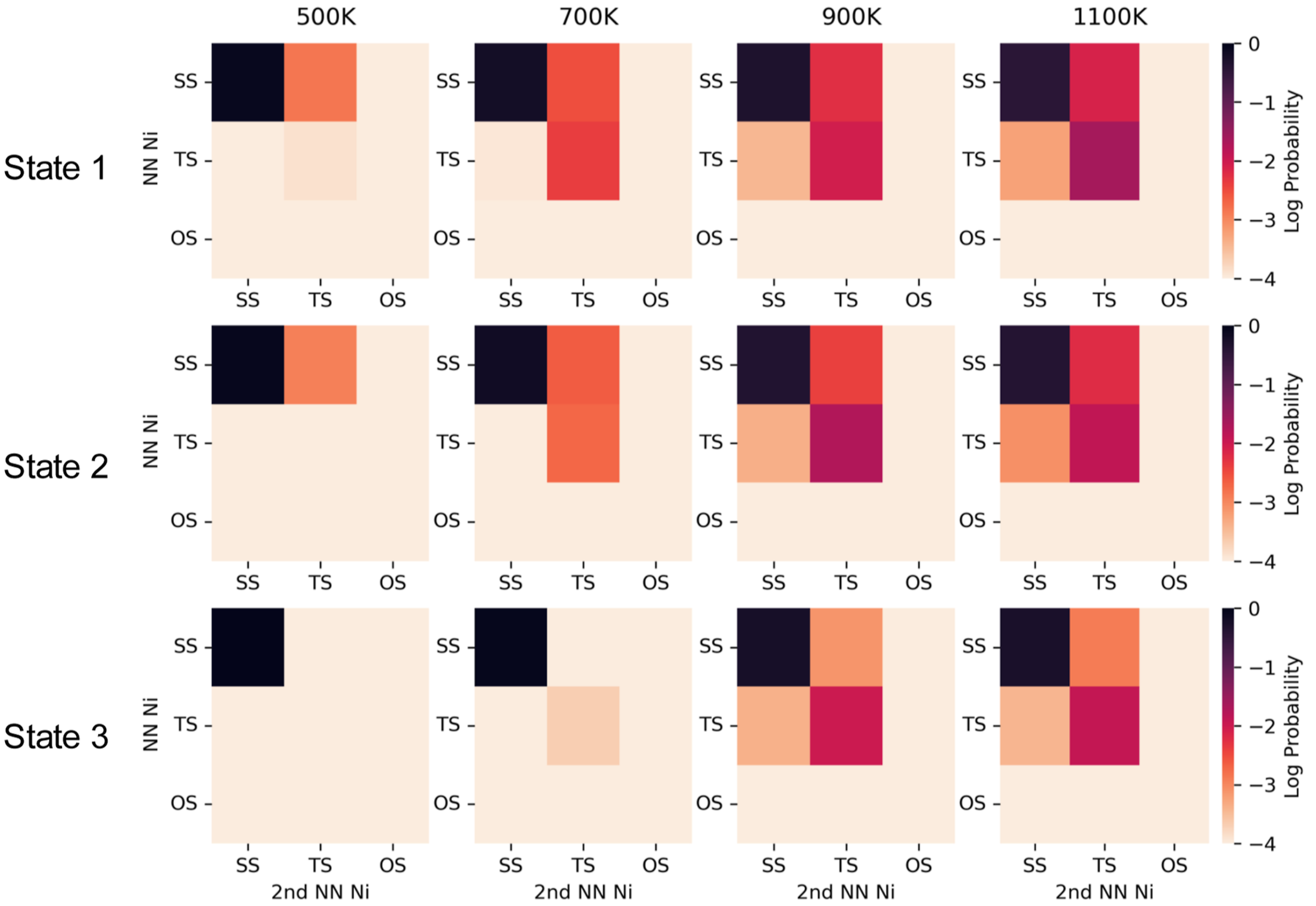

Figure 4. Logarithmic probability of the methane activated by particular nickel atom sites as the nearest and second nearest neighbor (NN) to the carbon atom. Each row corresponds to a specific state (states 1, 2, and 3) as defined in Figure 2. Nickel atoms are categorized as step site (SS), terrace site (TS), and other site (OS).

The transition state for MFEP2 is clearly visible at 500 K, but it disappears at higher temperatures (700, 900, and 1100 K). This is consistent with the behavior of the methyl group binding to a hollow site on Ni(511) at lower temperatures, which is not favored at higher temperatures. As the adsorbate binds to more surface nickel atoms, its mobility is likely reduced, diminishing its entropic advantage. Note that the enthalpies corresponding to the two paths are comparable, as shown in Figures S2 and 2H. Consequently, the entropic contributions to the free energy along the MFEP2 transition state become unfavorable at higher temperatures, causing the saddle point to no longer be identifiable on the FES's at higher temperatures.

The above analysis reveals that the structural diversity of active sites on the Ni(511) surface plays a crucial role on the thermodynamics of methane activation. We further examine in more detail the geometric and chemical characteristics of the Ni(511) surface, as depicted in Figure 1. This surface comprises a repeating array of step and terrace regions, with step-edge sites (SS) typically exhibiting under-coordination compared to terrace sites (TS) and other surface atoms (OS). These structural features directly influence the nature and distribution of adsorption sites for methane and its intermediates, as well as the entropic contributions that drive their stability. To gain a more detailed insight, we investigate the interactions of methane and methyl groups with the Ni(511) surface at different temperatures. Specifically, we identify and analyze their preferred adsorption sites by estimating the FES as a function of the *X*−*Y* coordinates of the carbon atom of the methane molecule or the adsorbed methyl. Such FESs, shown in Figure 3A, are the product of posthoc Spectral-ABF analysis through the same set of trajectories generated by the MLIP-MD with enhanced sampling. This approach minimizes the additional computational overhead needed to estimate the FES with respect to a new set of CVs without additional biasing potential. A detailed description of the approach can be found in the Methods section.

Figure 3 presents the spatial distribution of carbon atoms at the methane activation transition state (state 2 in Figure 2) within the *X*−*Y* plane on the Ni(511) surface, derived from the MLIP-MD simulation frames. The locations of step-site (SS), terrace-site (TS) and other-site (OS) nickel atoms are also highlighted for reference. Additionally, the figure displays the FES's as a function of the *X*−*Y* coordinates, illustrating the free energy variations of the binding of $[\mathrm{H}{-}CH_3]^{\ddagger}$ across different regions of the *X*−*Y* plane at 500, 700, and 900 K. At 500 K, carbon atoms at the transition state predominantly bind to the step-edge nickel atoms, with few instances of migration to terrace regions observed in the simulation frames. This preference is reflected in the FES at 500 K, where the step-edge region corresponds to a deeper energy minimum, and a significant free energy difference exists between the terrace and step-edge regions. Such a significant energy difference indicates

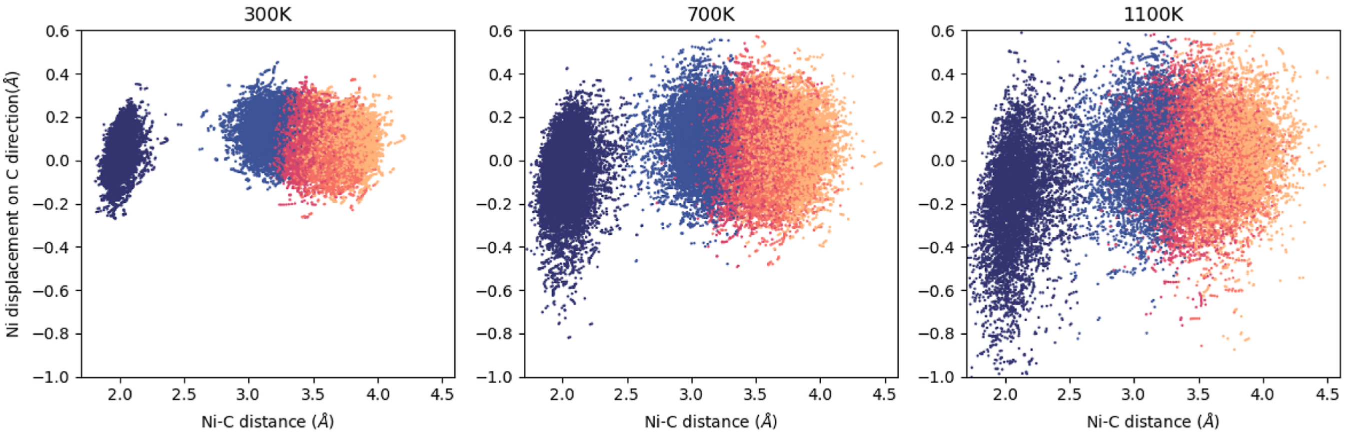

Figure 5. Correlation between Ni−C distance and Ni atom displacement along the Ni−C axis. Data points are collected from the transition state (state 2) along the minimum free energy path 1 (MFEP1). Nickel atom positions are color-coded based on their proximity to the carbon atom in methane, with colors indicating their rank from closest to farthest (blue = closest, orange = farthest); negative displacement values indicate that the nickel atom is moving toward the carbon atom.

that the binding of the transition state at the step edges is thermodynamically more favorable. This observation aligns with previous studies,[30,64] which suggest that methane dissociation preferentially occurs at stepped nickel sites due to their enhanced catalytic activity. As the temperature increases, the distribution of adsorption and activation sites broadens, with a noticeable increase in the number of frames showing carbon atoms located in terrace regions. Correspondingly, the free energy difference between the step-edge and terrace regions becomes narrower on the FES's at 700 and 900 K. This reduction in the free energy difference implies that the thermodynamic preference for the transition state binding to either region diminishes, allowing adsorption to occur more uniformly across the surface.

We further analyze the specific types of surface nickel atoms involved in methane activation by examining the molecular interactions along MFEP1, focusing on states 1 through 3. Figure 4 illustrates the probabilities of step-site (SS), terrace-site (TS), and other-site (OS) nickel atoms being the nearest and second nearest neighbors to the carbon atom of methane or the adsorbed methyl at temperatures ranging from 500 to 1100 K. At 500 K, the carbon atom consistently interacts with step-site nickel atoms, both as the nearest and second nearest neighbors, in nearly all simulation frames. However, at higher temperatures, there is a significant increase in the probability of terrace-site nickel atoms being both the nearest and second nearest neighbors to the carbon atom across states 1−3. This shift indicates that elevated temperatures facilitate methane activation at terrace sites, resulting in a more diverse distribution of active sites involved in the reaction.

To elucidate the molecular origins of the reduced free energy gap between the step and terrace regions for methane or methyl binding, we analyze the dynamic interactions of nickel atoms in the transition state of MFEP1. Figure 5 shows that in this transition state, the active nickel atom shifts out of the interface plane toward the carbon atom, lowering its coordination number with adjacent nickel atoms and creating a localized, under-coordinated environment that facilitates the C−H bond cleavage. The displacement of the active nickel atom is strongly correlated with the Ni−C distance at all temperatures, with the extent of elevation increasing as the temperature increases. Additionally, Figure 5 indicates that nickel atoms farther away from carbon do not exhibit this reconstructive response, showing no significant change in their position or coordination as the C−H bond breaks. This temperature-dependent elevation of the active Ni atom reflects the increased flexibility of the Ni(511) surface under thermal fluctuations. At elevated temperatures, Ni atoms are more sensitive to the breaking of the C−H bond and can slightly reconstruct even on terrace sites, thereby reducing the free energy barriers for methane/methyl binding. This dynamic reconstruction narrows the free energy gap between step and terrace regions, and in turn broadens the range of active sites available for methane activation at higher temperatures.

3. CONCLUSION

In this study, we have presented a detailed molecular-level investigation of methane activation on the Ni(511) surface under realistic operando conditions, using MLIP combined with enhanced sampling techniques. Our simulations reveal that the Ni(511) surface, characterized by its diverse array of atomic environments, exhibits unique reactivity trends for methane activation.

At the molecular level, methane initially interacts dynamically with step-edge nickel atoms, coordinating both its carbon and hydrogen atoms to these under-coordinated sites. This early stage coordination leads to a slight increase in enthalpy as a result of the repulsion between a nearly intact methane molecule with the surface but results in a significant decrease in entropy, attributed to the restricted mobility of the methane molecule upon binding. As the reaction progresses past the transition state, the mobility of the adsorbed species increases, leading to substantial entropy gains. However, when CH_x species (where x = 3 or 4) bind to multiple surface nickel atoms, such as in bridge or hollow sites, their mobility is further restricted, causing a decrease in entropy. This entropic penalty explains why certain configurations, although energetically favorable in terms of enthalpy, are not observed in the free energy landscapes at higher temperatures. Similarly, our analysis uncovers two primary activation routes: a dominant single-nickel activation mechanism at step-edge sites and a secondary route involving cooperative activation by two nickel atoms. The second one becomes less favorable at elevated temperatures due to entropic contributions that increase the free energy barrier, causing it to disappear from the free energy surfaces beyond 700 K. This highlights the critical role of

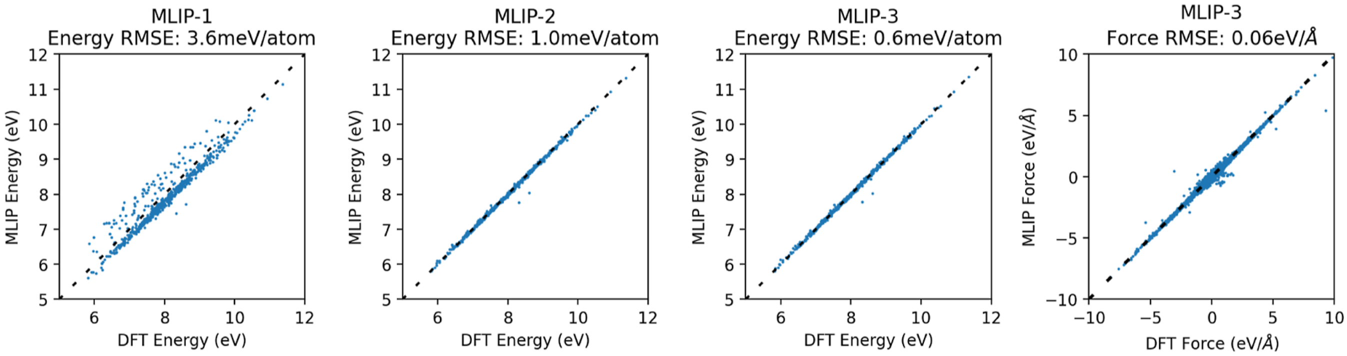

Figure 6. Energy predicted by DFT calculations versus those generated by MLIP-1, MLIP-2, and MLIP-3, and force comparison for MLIP-3.

entropy in determining the preferred activation route under different temperatures. Importantly, our findings demonstrate that at higher temperatures, methane activation is not limited to step-edge sites, but extends to terrace sites as well. Elevated temperatures reduce the free energy barriers associated with the adsorbates migrating from the step to terrace sites, and enhanced thermal fluctuations increase the surface dynamics. This leads to a broader distribution of active sites, reflecting the adaptive and transient nature of catalytic sites under operando conditions.

Using MLIPs combined with enhanced sampling methods, we can separate enthalpic and entropic contributions to the activation of methane on a relatively complex surface with a higher Miller index. This approach provides helpful insights into surface reactivity and reaction dynamics at realistic temperatures. Our work underscores the importance of considering both the static structural features of catalytic surfaces and their dynamic, temperature-dependent behaviors when designing efficient catalysts. We have focused here on a case study relevant to catalytic methane activation and established a methodological workflow that can be adapted to different bond-breaking processes catalyzed by various metals, alloys, or more intricate catalysts. Our study highlights the power of machine learning-based approaches to accurately capture the interplay of enthalpic and entropic contributions, surface reactivity, and reaction dynamics at realistic length and time scales, and under relevant reaction conditions. Our models offer microscopic insights that can provide a foundation for the rational design of more efficient catalysts that could be potentially capable of operating under milder conditions. Future work may extend this approach to explore other complex catalytic systems, offering a pathway toward addressing critical challenges in sustainable chemical transformations.

4. METHODS

4.1. First-Principles Calculations. DFT calculations are performed using the Vienna ab initio simulation package (VASP, version 6.3.2).[65−69] A periodic, five-layer Ni(511) surface is prepared with the two lowest layers fixed to simulate the bulk structure (unit cell shown in Figure 1). A 10 Å vacuum space is added in the z dimension to minimize the periodic image interaction in that direction. All DFT simulations are conducted with spin polarization enabled. We employ the BEEF-vdW exchange−correlation functional in conjunction with projector-augmented wave (PAW) pseudopotentials.[69−71] A plane-wave energy cutoff of 400 eV is set, and the electronic self-consistency is achieved with a convergence criterion of 10^{-4} eV. The Brillouin zone is sampled using a Monkhorst-Pack k-point grid of 2 × 2 × 1. A Fermi smearing scheme is applied.

4.2. Machine-Learned Interatomic Potentials. The Allegro framework[72] is employed to train the MLIP that captures interactions among nickel, carbon, and hydrogen atoms. The contribution of each atom is modeled using an equivariant neural network. The network begins by embedding the local relative atomic positions into spherical harmonics, creating a representation of the environment of each atom. This embedding is then processed through tensor product layers to yield a single scalar representing its potential energy contribution. The total potential energy of a given configuration is computed as the sum of energy contribution of each atom, based on their local atomic environments within a cutoff radius. In our experiments, an embedding layer with spherical harmonics is used and a cutoff radius of 6.0 Å is set. Our model incorporates two layers of the tensor product, each containing 64, 128, 256, and 512 neurons, respectively.

4.3. Validation of MLIPs and Effect of Active Learning. We monitor and validate the accuracy of the machine learning interatomic potential (MLIP).[73,74] Building on our previous study of methane activation on the Ni(111) surface,[60] we employ active learning to iteratively refine MLIP, resulting in three models: MLIP-1, MLIP-2, and MLIP-3 (see Section 4.7 for more details). Figure 6 compares the predicted forces and energies of MLIP with the ground truth values calculated by DFT. Each scatterplot point represents the force or energy of a frame from a trajectory generated using the current MLIP iteration (MLIP-X) with molecular dynamics and enhanced sampling. The selected frames are uniformly distributed throughout the space of collective variables.[60] For MLIP-3, the predicted forces and energies show high correlations with the DFT results, with correlation coefficients of 0.999 and 0.998, respectively. The root mean squared errors (RMSEs) are 0.5 meV/atom for energy and 0.06 eV/Å for force, both below the commonly accepted chemical accuracy threshold of 1 kcal/mol.[75] The comparison of MLIP-1, MLIP-2, and MLIP-3 demonstrates that iterative refinement through active learning progressively reduces prediction errors for both energy and force.

4.4. Molecular Dynamics Simulations. We perform classical MD simulations using the Atomic Simulation Environment (ASE) framework,[76] integrated with the Allegro[72] and PySAGES[77] packages for enhanced sampling. To efficiently explore the free energy landscape of methane activation, we discretize the CV space into a 5 × 5 grid, with each grid window further subdivided into 30 bins per axis.

Initial configurations are prepared by applying harmonic biasing to confine the system within the designated CV range. In the next step, we perform MD simulations using the Spectral-ABF enhanced sampling method.[77] Simulations are carried out at temperatures of 500, 700, 900, and 1100 K, with a time step of 0.25 fs for 2,000,000 steps per CV window, for a total simulation time of 12.5 ns. The MD simulations are controlled by Langevin thermostat (friction coefficient: 10 ps^{-1}).

4.5. Free Energy Calculations with Enhanced Sampling.

We use Spectral-Adaptive Biasing Force (Spectral-ABF)[61] as our enhanced sampling technique to estimate the free energy surface of the methane-nickel system. As a method of the ABF family.[78,79] Spectral-ABF gradually builds an estimate of the gradient of the free energy which is applied as biasing force to the system. In the long-time limit, this biasing force ensures good sampling in the chosen CV space—assuming the CVs roughly correspond to the slowest dynamical modes of the system. The starting point of adaptive biasing force methods is to compute the gradient of the free energy. Spectral-ABF uses the expression proposed by Darve, et al.[79]

$$F_{\text{bias}} = -\frac{\mathrm{d}A(\xi)}{\mathrm{d}\xi} = \left\langle \frac{\mathrm{d}}{\mathrm{d}t}(W\cdot p) \middle| \xi \right\rangle \tag{1}$$

where $A(\xi)$ represents the free energy given collective variable ξ, W represents the inverse of the jacobian of ξ as a function of the positions of all atoms in the system ($W\cdot\nabla\xi = I$), p represents the momenta of all atoms, and $\langle\circ|\xi\rangle$ means conditional average. The applied force acts opposite to the gradient of the underlying free energy, enabling the system to explore the collective variable (CV) space in a manner analogous to free diffusion once the method converges.

Formally, the gradient of the free energy surface $A(\xi^*)$ corresponds to the average gradient of the Hamiltonian, H, at ξ^*.

$$\frac{\mathrm{d}A(\xi^*)}{\mathrm{d}\xi} = \left\langle \frac{\mathrm{d}H}{\mathrm{d}\xi} \middle| \xi = \xi^* \right\rangle \tag{2}$$

In practice, we separate the CV space into bins, such that the condition $\xi = \xi^*$ is relaxed as ξ falls into the same bin as the center of the bin ξ^*. Spectral-ABF models the free energy landscape of the system as a basis expansion whose gradient matches the gradient of the free energy $\frac{\mathrm{d}A(\xi^*)}{\mathrm{d}\xi}$ computed in a simulation. For our experiments in a single window, we use a grid of [8, 8] bins, and for the final combined FES estimation, we expand the grid to [64, 64] bins. We choose Chebyshev polynomials for the basis expansion. Compared to other enhanced sampling methods, Spectral-ABFconverges reasonably faster.[77]

4.6. Posthoc Spectral-ABF Analysis.

Although original Spectral-ABF enables fast sampling across complex CV spaces, it is limited to producing free energy surface estimates with respect to the initially designated CVs, typically restricted to one or two because the binning strategy suffers from the curse of dimensionality. This constraint means that important information—such as the location of active sites for our system of study—may be omitted from the set of chosen CVs. Rerunning simulations to study the free energy as a function of different CV combinations can be computationally expensive. This can usually be addressed by performing a reweighted estimation estimation of the free energy. In this work, instead of reweighting, we perform a posthoc analysis using Spectral-ABF on existing trajectories to directly reconstruct the free energy surface with new CVs. First, we estimate the gradient of the free energy with respect to the new CVs ξ_{new}, similar to eq 2.

$$\frac{\mathrm{d}A(\xi^*_{\text{new}})}{\mathrm{d}\xi_{\text{new}}} = \left\langle \frac{\mathrm{d}H}{\mathrm{d}\xi_{\text{new}}} \middle| \xi_{\text{new}} = \xi^*_{\text{new}} \right\rangle \tag{3}$$

In eq 3, H is the Halmiltonian derived from the trajectories generated from the MLIP-MD enhanced sampling simulations. Given that our collective variable of interest is the $X-Y$ coordinate of methane, we discretize both major axes of the box into 40 segments, yielding a grid of 1600 points. Recognizing that the nickel surface exhibits cyclic symmetry—where each row of nickel atoms is equivalent—we conceptualize the surface as a series of five repeating parallelograms. The x-axis length of each parallelogram is 11.43 Å, while the y-axis is tilted with vector components (1.36, 2.09 Å). We then average the gradient data collected from these five parallelograms to produce a grid of gradient estimates with dimensions (40, 8). To reconstruct the full $X-Y$ surface, we tile these estimates five times, preserving the cyclic nature of the surface. Since our experiments were unbiased with respect to the $X-Y$ coordinate, they may suffer from undersampling in low-energy regions. By leveraging surface symmetry, our postprocessing method increases accuracy by incorporating more data from the available trajectories.

4.7. MLIP Training and Active Learning.

MLIP training process typically requires a curated and representative set of configurations, where energy and force data are generated through DFT calculations. However, constructing such a representative set can be challenging, particularly in complex interfacial systems like the Ni(511) system in this work. Therefore, we use an active learning pipeline[60,80] to iteratively update the training set and the MLIP to ensure the validity of the model. To initialize the MLIP training set, we use an existing methane-nickel MLIP model developed for the Ni(111) surface,[60] which we refer to as MLIP-0. This model is chosen because it captures methane-Ni interactions effectively. However, because it has not encountered the undercoordinated nickel atoms, it may not adequately describe methane interactions with step edges. For an extensive sampling, we employ the same setting described in Subsection 4.4 to partition the CV space into a 5 × 5 grid. We then conduct Spectral-ABF simulations within each grid cell. Subsequently, k-means clustering is applied to segment the simulation trajectory in each window within the CV space, selecting frames nearest to cluster centers as representative configurations. These configurations are used for DFT calculations, forming the training set for our initial MLIP model, MLIP-1. We train this model using the parameters detailed in Subsection 4.2. We refer to the entire sequence—simulation, configuration generation, and training—as an iteration. We complete the X iterations to yield a series of MLIP-X models, where X = 1, 2, and 3. In subsequent iterations ($X > 1$), we refine the training set by selecting only frames exhibiting significant energy prediction discrepancies between MLIP and DFT calculations. This selection strategy emphasizes previously unseen cases by the MLIP model, enhancing the model performance on those configurations.

4.8. Collective Variables Definition. To effectively model methane activation on the Ni(511) surface, we define CVs that describe the progression from initial physisorption through the transition state to the fully activated state where the C−H bond is broken. Specifically, we define coordination numbers between the carbon and hydrogen atoms ($\xi_{\mathrm{C-H}}$) and between the carbon and surface nickel atoms ($\xi_{\mathrm{C-Ni}}$) to quantify the different types of interactions between methane and the Ni(511) surface. These coordination numbers are calculated using smooth switching functions to ensure continuity and differentiability.

The CVs are formally defined as

$$\xi_{\mathrm{C-Ni}} = \sum_{i}^{N_{\mathrm{Ni}}} \frac{1 - (R(\mathrm{C},\mathrm{Ni}_i)/R_0)^9}{1 - (R(\mathrm{C},\mathrm{Ni}_i)/R_0)^{21}} \tag{4}$$

$$\xi_{\mathrm{C-H}} = \sum_{j}^{N_{\mathrm{H}}} \frac{1 - (R(\mathrm{C},\mathrm{H}_j)/R_1)^9}{1 - (R(\mathrm{C},\mathrm{H}_j)/R_1)^{14}} \tag{5}$$

In these equations, $R(\mathrm{C},\mathrm{Ni}_i)$ represents the distance between the carbon atom and the i-th nickel atom on the surface, calculated under the minimum image convention. Similarly, $R(\mathrm{C},\mathrm{H}_j)$ denotes the distance between the carbon atom and the j-th hydrogen atom. We increase the exponent in the denominator for $\xi_{\mathrm{C-Ni}}$ to better distinguish surface bonds, enhancing the sensitivity of the CV to changes in coordination. The cutoff distances are set to R_0 = 2.6 Å for C−Ni interactions and R_1 = 1.6 Å for C−H interactions, respectively. A visualization of these CV definitions is provided in the Supporting Information.

■ ASSOCIATED CONTENT

Data Availability Statement

The authors declare that the data supporting the findings of this study are available within the paper and its Supporting Information files.

SI Supporting Information

The Supporting Information is available free of charge at https://pubs.acs.org/doi/10.1021/acscatal.5c00724.

> Implementation details of the AutoNEB algorithm; free energy surface at 1100 K; comparison of minimum free energy and enthalpy paths; convergence analysis of enhanced sampling calculations; integration of gradient information from multiple sampling windows; quantification of nickel atom elevation in transition states (PDF)

■ AUTHOR INFORMATION

Corresponding Authors

Yinan Xu − *Pritzker School of Molecular Engineering, The University of Chicago, Chicago, Illinois 60637, United States;* orcid.org/0000-0002-5824-3502; Email: xuyinan@uchicago.edu

Juan J. de Pablo − *Department of Chemical and Biomolecular Engineering, Tandon School of Engineering, New York University, Brooklyn, New York 11201, United States; Courant Institute of Mathematical Sciences, New York University, New York, New York 10012, United States; Department of Physics, New York University, New York, New York 10003, United States;* orcid.org/0000-0002-3526-516X; Email: jjd8110@nyu.edu

Authors

Yezhi Jin − *Pritzker School of Molecular Engineering, The University of Chicago, Chicago, Illinois 60637, United States*

Jireh S. García Sánchez − *Pritzker School of Molecular Engineering, The University of Chicago, Chicago, Illinois 60637, United States*

Gustavo R. Pérez-Lemus − *Pritzker School of Molecular Engineering, The University of Chicago, Chicago, Illinois 60637, United States*

Pablo F. Zubieta Rico − *Pritzker School of Molecular Engineering, The University of Chicago, Chicago, Illinois 60637, United States;* orcid.org/0000-0002-1211-4836

Massimiliano Delferro − *Chemical Sciences and Engineering Division, Argonne National Laboratory, Lemont, Illinois 60439, United States;* orcid.org/0000-0002-4443-165X

Complete contact information is available at: https://pubs.acs.org/10.1021/acscatal.5c00724

Author Contributions

[#]These authors contributed equally to this work: Yezhi Jin and Yinan Xu.

Notes

The authors declare no competing financial interest.

■ ACKNOWLEDGMENTS

The authors are grateful to Prof. Laura Gagliardi for helpful discussions. This work was supported by the Catalyst Design for Decarbonization Center, an Energy Frontier Research Center (EFRC) funded by the U.S. Department of Energy, Office of Science, Basic Energy Sciences (DE-SC0023383). Y.J. is grateful for a training award from the National Science Foundation under NRT Grant no. 2022023. The development of the PySAGES code and the advanced sampling methods used for this work are supported by the Midwest Integrated Center for Computational Materials Design (MICCoM), funded by the Department of Energy, Office of Science, Basic Energy Sciences, Division of Materials Science and Engineering. The authors also acknowledge the computational resources provided by Argonne National Laboratory and by the Research Computing Center at the University of Chicago.

■ REFERENCES

(1) Shindell, D. T.; Faluvegi, G.; Koch, D. M.; Schmidt, G. A.; Unger, N.; Bauer, S. E. Improved Attribution of Climate Forcing to Emissions. *Science* **2009**, *326*, 716−718.

(2) Li, Q.; Ouyang, Y.; Li, H.; Wang, L.; Zeng, J. Photocatalytic conversion of methane: recent advancements and prospects. *Angew. Chem., Int. Ed.* **2022**, *61*, No. e202108069.

(3) Elvidge, C. D.; Bazilian, M. D.; Zhizhin, M.; Ghosh, T.; Baugh, K.; Hsu, F.-C. The potential role of natural gas flaring in meeting greenhouse gas mitigation targets. *Energy Strat. Rev.* **2018**, *20*, 156−162.

(4) He, L.; Fan, Y.; Bellettre, J.; Yue, J.; Luo, L. A review on catalytic methane combustion at low temperatures: Catalysts, mechanisms, reaction conditions and reactor designs. *Renew. Sustain. Energy Rev.* **2020**, *119*, 109589.

(5) Schwach, P.; Pan, X.; Bao, X. Direct Conversion of Methane to Value-Added Chemicals over Heterogeneous Catalysts: Challenges and Prospects. *Chem. Rev.* **2017**, *117*, 8497−8520.

(6) Zain, M. M.; Mohamed, A. R. An overview on conversion technologies to produce value added products from CH4 and CO2 as major biogas constituents. *Renew. Sustain. Energy Rev.* **2018**, *98*, 56−63.

(7) Xie, S.; Lin, S.; Zhang, Q.; Tian, Z.; Wang, Y. Selective electrocatalytic conversion of methane to fuels and chemicals. *J. Energy Chem.* **2018**, *27*, 1629−1636.

(8) Liu, Z.; Huang, E.; Orozco, I.; Liao, W.; Palomino, R. M.; Rui, N.; Duchoň, T.; Nemšák, S.; Grinter, D. C.; Mahapatra, M.; et al. Water-promoted interfacial pathways in methane oxidation to methanol on a CeO $_2$ -Cu $_2$ O catalyst. *Science* **2020**, *368*, 513−517.

(9) Zuo, Z.; Ramírez, P. J.; Senanayake, S. D.; Liu, P.; Rodriguez, J. A. Low-temperature conversion of methane to methanol on CeO x/Cu2O catalysts: water controlled activation of the C−H bond. *J. Am. Chem. Soc.* **2016**, *138*, 13810−13813.

(10) Narsimhan, K.; Iyoki, K.; Dinh, K.; Román-Leshkov, Y. Catalytic oxidation of methane into methanol over copper-exchanged zeolites with oxygen at low temperature. *ACS Cent. Sci.* **2016**, *2*, 424−429.

(11) Grundner, S.; Markovits, M. A.; Li, G.; Tromp, M.; Pidko, E. A.; Hensen, E. J.; Jentys, A.; Sanchez-Sanchez, M.; Lercher, J. A. Single-site trinuclear copper oxygen clusters in mordenite for selective conversion of methane to methanol. *Nat. Commun.* **2015**, *6*, 7546.

(12) Tomkins, P.; Ranocchiari, M.; van Bokhoven, J. A. Direct Conversion of Methane to Methanol under Mild Conditions over Cu-Zeolites and beyond. *Acc. Chem. Res.* **2017**, *50*, 418−425.

(13) Han, B.; Yang, Y.; Xu, Y.; Etim, U.; Qiao, K.; Xu, B.; Yan, Z. A review of the direct oxidation of methane to methanol. *Chin. J. Catal.* **2016**, *37*, 1206−1215.

(14) Shan, J.; Li, M.; Allard, L. F.; Lee, S.; Flytzani-Stephanopoulos, M. Mild oxidation of methane to methanol or acetic acid on supported isolated rhodium catalysts. *Nature* **2017**, *551*, 605−608.

(15) Sushkevich, V. L.; Palagin, D.; Ranocchiari, M.; van Bokhoven, J. A. Selective anaerobic oxidation of methane enables direct synthesis of methanol. *Science* **2017**, *356*, 523−527.

(16) Abdulrasheed, A.; Jalil, A. A.; Gambo, Y.; Ibrahim, M.; Hambali, H. U.; Shahul Hamid, M. Y. A review on catalyst development for dry reforming of methane to syngas: Recent advances. *Renew. Sustain. Energy Rev.* **2019**, *108*, 175−193.

(17) Arman, A.; Hagos, F.; Abdullah, A.; Mamat, R.; Aziz, A.; Cheng, C. Syngas production through steam and CO2 reforming of methane over Ni-based catalyst-A Review. *IOP Conf. Ser.:Mater. Sci. Eng.* **2020**, *736*, 042032.

(18) Wei, J.; Iglesia, E. Isotopic and kinetic assessment of the mechanism of reactions of CH4 with CO2 or H2O to form synthesis gas and carbon on nickel catalysts. *J. Catal.* **2004**, *224*, 370−383.

(19) Olah, G. A.; Goeppert, A.; Czaun, M.; Mathew, T.; May, R. B.; Prakash, G. K. S. Single Step Bi-reforming and Oxidative Bi-reforming of Methane (Natural Gas) with Steam and Carbon Dioxide to Metgas (CO-2H2) for Methanol Synthesis: Self-Sufficient Effective and Exclusive Oxygenation of Methane to Methanol with Oxygen. *J. Am. Chem. Soc.* **2015**, *137*, 8720−8729.

(20) da Silva, M. J. Synthesis of methanol from methane: Challenges and advances on the multi-step (syngas) and one-step routes (DMTM). *Fuel Process. Technol.* **2016**, *145*, 42−61.

(21) Aziz, M.; Setiabudi, H.; Teh, L.; Annuar, N.; Jalil, A. A review of heterogeneous catalysts for syngas production via dry reforming. *J. Taiwan Inst. Chem. Eng.* **2019**, *101*, 139−158.

(22) Fan, M.; Abdullah, A. Z.; Bhatia, S. Catalytic Technology for Carbon Dioxide Reforming of Methane to Synthesis Gas. *ChemCatChem* **2009**, *1*, 192−208.

(23) Han, B.; Wang, F.; Zhang, L.; Wang, Y.; Fan, W.; Xu, L.; Yu, H.; Li, Z. Syngas production from methane steam reforming and dry reforming reactions over sintering-resistant Ni@SiO2 catalyst. *Res. Chem. Intermed.* **2020**, *46*, 1735−1748.

(24) Liu, Z.; Lustemberg, P.; Gutiérrez, R. A.; Carey, J. J.; Palomino, R. M.; Vorokhta, M.; Grinter, D. C.; Ramírez, P. J.; Matolín, V.; Nolan, M. In situ investigation of methane dry reforming on metal/ceria (111) surfaces: metal−support interactions and C- H bond activation at low temperature. *Angew. Chem., Int. Ed.* **2017**, *56*, 13041−13046.

(25) Wei, J.; Iglesia, E. Mechanism and site requirements for activation and chemical conversion of methane on supported Pt clusters and turnover rate comparisons among noble metals. *J. Phys. Chem. B* **2004**, *108*, 4094−4103.

(26) Bengaard, H. S.; Nørskov, J. K.; Sehested, J.; Clausen, B.; Nielsen, L.; Molenbroek, A.; Rostrup-Nielsen, J. Steam reforming and graphite formation on Ni catalysts. *J. Catal.* **2002**, *209*, 365−384.

(27) Aparicio, L. Transient isotopic studies and microkinetic modeling of methane reforming over nickel catalysts. *J. Catal.* **1997**, *165*, 262−274.

(28) Chin, Y.-H. C.; King, D. L.; Roh, H.-S.; Wang, Y.; Heald, S. M. Structure and reactivity investigations on supported bimetallic AuNi catalysts used for hydrocarbon steam reforming. *J. Catal.* **2006**, *244*, 153−162.

(29) Niu, J.; Liland, S. E.; Yang, J.; Rout, K. R.; Ran, J.; Chen, D. Effect of oxide additives on the hydrotalcite derived Ni catalysts for CO2 reforming of methane. *Chem. Eng. J.* **2019**, *377*, 119763.

(30) Abild-Pedersen, F.; Greeley, J.; Nørskov, J. K. Understanding the Effect of Steps, Strain, Poisons, and Alloying: Methane Activation on Ni Surfaces. *Catal. Lett.* **2005**, *105*, 9−13.

(31) Latimer, A. A.; Aljama, H.; Kakekhani, A.; Yoo, J. S.; Kulkarni, A.; Tsai, C.; Garcia-Melchor, M.; Abild-Pedersen, F.; Nørskov, J. K. Mechanistic insights into heterogeneous methane activation. *Phys. Chem. Chem. Phys.* **2017**, *19*, 3575−3581.

(32) Liu, G.; Shih, A. J.; Deng, H.; Ojha, K.; Chen, X.; Luo, M.; McCrum, I. T.; Koper, M. T. M.; Greeley, J.; Zeng, Z. Site-specific reactivity of stepped Pt surfaces driven by stress release. *Nature* **2024**, *626*, 1005−1010.

(33) Tu, W.; Ghoussoub, M.; Singh, C. V.; Chin, Y.-H. C. Consequences of Surface Oxophilicity of Ni, Ni-Co, and Co Clusters on Methane Activation. *J. Am. Chem. Soc.* **2017**, *139*, 6928−6945.

(34) Wei, J.; Iglesia, E. Structural and Mechanistic Requirements for Methane Activation and Chemical Conversion on Supported Iridium Clusters. *Angew. Chem., Int. Ed.* **2004**, *43*, 3685−3688.

(35) Jones, G.; Jakobsen, J. G.; Shim, S. S.; Kleis, J.; Andersson, M. P.; Rossmeisl, J.; Abild-Pedersen, F.; Bligaard, T.; Helveg, S.; Hinnemann, B. others First principles calculations and experimental insight into methane steam reforming over transition metal catalysts. *J. Catal.* **2008**, *259*, 147−160.

(36) Zhao, Z.-J.; Chiu, C.-c.; Gong, J. Molecular understandings on the activation of light hydrocarbons over heterogeneous catalysts. *Chem. Sci.* **2015**, *6*, 4403−4425.

(37) Yu, Y.-X.; Yang, J.; Zhu, K.-K.; Sui, Z.-J.; Chen, D.; Zhu, Y.-A.; Zhou, X.-G. High-Throughput Screening of Alloy Catalysts for Dry Methane Reforming. *ACS Catal.* **2021**, *11*, 8881−8894.

(38) Xu, Y.; Lausche, A. C.; Wang, S.; Khan, T. S.; Abild-Pedersen, F.; Studt, F.; Nørskov, J. K.; Bligaard, T. In silico search for novel methane steam reforming catalysts. *New J. Phys.* **2013**, *15*, 125021.

(39) Zhu, Y.-A.; Chen, D.; Zhou, X.-G.; Yuan, W.-K. DFT studies of dry reforming of methane on Ni catalyst. *Catal. Today* **2009**, *148*, 260−267.

(40) Liang, Z.; Li, T.; Kim, M.; Asthagiri, A.; Weaver, J. F. Low-temperature activation of methane on the IrO2 (110) surface. *Science* **2017**, *356*, 299−303.

(41) Ishikawa, A.; Tateyama, Y. What Is the Active Site for the Oxidative Coupling of Methane Catalyzed by MgO? A Metadynamics-Biased Ab Initio Molecular Dynamics Study. *J. Phys. Chem. C* **2020**, *124*, 6054−6062.

(42) Ghoussoub, M.; Yadav, S.; Ghuman, K. K.; Ozin, G. A.; Singh, C. V. Metadynamics-Biased ab Initio Molecular Dynamics Study of Heterogeneous CO2 Reduction via Surface Frustrated Lewis Pairs. *ACS Catal.* **2016**, *6*, 7109−7117.

(43) Ma, C.; Piccinin, S.; Fabris, S. Reaction Mechanisms of Water Splitting and H2 Evolution by a Ru(II)-Pincer Complex Identified with Ab Initio Metadynamics Simulations. *ACS Catal.* **2012**, *2*, 1500−1506.

(44) Lee, E. M. Y.; Ludwig, T.; Yu, B.; Singh, A. R.; Gygi, F.; Nørskov, J. K.; de Pablo, J. J. Neural Network Sampling of the Free Energy Landscape for Nitrogen Dissociation on Ruthenium. *J. Phys. Chem. Lett.* **2021**, *12*, 2954−2962.

(45) Mortazavi, B.; Zhuang, X.; Rabczuk, T.; Shapeev, A. V. Atomistic modeling of the mechanical properties: the rise of machine learning interatomic potentials. *Mater. Horiz.* **2023**, *10*, 1956−1968.

(46) Deringer, V. L.; Caro, M. A.; Csányi, G. Machine learning interatomic potentials as emerging tools for materials science. *Adv. Mater.* **2019**, *31*, 1902765.

(47) Sauer, J. The future of computational catalysis. *J. Catal.* **2024**, *433*, 115482.

(48) Batatia, I.; Kovacs, D. P.; Simm, G.; Ortner, C.; Csányi, G. MACE: Higher order equivariant message passing neural networks for fast and accurate force fields. *Adv. Neural Inf. Process. Syst.* **2022**, *35*, 11423−11436.

(49) Unke, O. T.; Meuwly, M. PhysNet: A neural network for predicting energies, forces, dipole moments, and partial charges. *J. Chem. Theory Comput.* **2019**, *15*, 3678−3693.

(50) Behler, J.; Parrinello, M. Generalized neural-network representation of high-dimensional potential-energy surfaces. *Phys. Rev. Lett.* **2007**, *98*, 146401.

(51) Zhang, L.; Han, J.; Wang, H.; Car, R.; Weinan, E. Deep potential molecular dynamics: a scalable model with the accuracy of quantum mechanics. *Phys. Rev. Lett.* **2018**, *120*, 143001.

(52) Vandermause, J.; Torrisi, S. B.; Batzner, S.; Xie, Y.; Sun, L.; Kolpak, A. M.; Kozinsky, B. On-the-fly active learning of interpretable Bayesian force fields for atomistic rare events. *npj Comput. Mater.* **2020**, *6*, 20.

(53) Qiao, Z.; Christensen, A. S.; Welborn, M.; Manby, F. R.; Anandkumar, A.; Miller, T. F. Informing geometric deep learning with electronic interactions to accelerate quantum chemistry. *Proc. Natl. Acad. Sci. U.S.A.* **2022**, *119*, No. e2205221119.

(54) Schütt, K. T.; Sauceda, H. E.; Kindermans, P.-J.; Tkatchenko, A.; Müller, K. R. Schnet−a deep learning architecture for molecules and materials. *J. Chem. Phys.* **2018**, *148*, 241722.

(55) Maxson, T.; Soyemi, A.; Chen, B. W. J.; Szilvási, T. Enhancing the Quality and Reliability of Machine Learning Interatomic Potentials through Better Reporting Practices. *J. Phys. Chem. C* **2024**, *128*, 6524−6537.

(56) Chen, B. W. J.; Mavrikakis, M. Modeling the impact of structure and coverage on the reactivity of realistic heterogeneous catalysts. *Nat. Chem. Eng.* **2025**, *2*, 181−197.

(57) Bonati, L.; Polino, D.; Pizzolitto, C.; Biasi, P.; Eckert, R.; Reitmeier, S.; Schlögl, R.; Parrinello, M. The role of dynamics in heterogeneous catalysis: Surface diffusivity and N2 decomposition on Fe (111). *Proc. Natl. Acad. Sci. U.S.A.* **2023**, *120*, No. e2313023120.

(58) Tripathi, S.; Bonati, L.; Perego, S.; Parrinello, M. How Poisoning Is Avoided in a Step of Relevance to the Haber−Bosch Catalysis. *ACS Catal.* **2024**, *14*, 4944−4950.

(59) Perego, S.; Bonati, L.; Tripathi, S.; Parrinello, M. How dynamics changes ammonia cracking on iron surfaces. *ACS Catal.* **2024**, *14*, 14652−14664.

(60) Xu, Y.; Jin, Y.; García Sánchez, J. S.; Pérez-Lemus, G. R.; Zubieta Rico, P. F.; Delferro, M.; de Pablo, J. J. A Molecular View of Methane Activation on Ni (111) through Enhanced Sampling and Machine Learning. *J. Phys. Chem. Lett.* **2024**, *15*, 9852−9862.

(61) Zubieta Rico, P. F.; Pérez-Lemus, G. R.; de Pablo, J. J. Efficient sampling of free energy landscapes with functions in Sobolev spaces. *J. Chem. Phys.* **2025**, *162*, 084109.

(62) Kolsbjerg, E. L.; Groves, M. N.; Hammer, B. An automated nudged elastic band method. *J. Chem. Phys.* **2016**, *145*, 094107.

(63) Henkelman, G.; Uberuaga, B. P.; Jónsson, H. A climbing image nudged elastic band method for finding saddle points and minimum energy paths. *J. Chem. Phys.* **2000**, *113*, 9901−9904.

(64) Arevalo, R. L.; Aspera, S. M.; Escaño, M. C. S.; Nakanishi, H.; Kasai, H. Tuning methane decomposition on stepped Ni surface: The role of subsurface atoms in catalyst design. *Sci. Rep.* **2017**, *7*, 13963.

(65) Kresse, G.; Furthmüller, J. Efficient iterative schemes for ab initio total-energy calculations using a plane-wave basis set. *Phys. Rev. B:Condens. Matter Mater. Phys.* **1996**, *54*, 11169−11186.

(66) Kresse, G.; Furthmüller, J. Efficiency of ab-initio total energy calculations for metals and semiconductors using a plane-wave basis set. *Comput. Mater. Sci.* **1996**, *6*, 15−50.

(67) Kresse, G.; Hafner, J. Ab initio molecular dynamics for liquid metals. *Phys. Rev. B:Condens. Matter Mater. Phys.* **1993**, *47*, 558−561.

(68) Kresse, G.; Hafner, J. Ab initio molecular-dynamics simulation of the liquid-metal−amorphous-semiconductor transition in germanium. *Phys. Rev. B:Condens. Matter Mater. Phys.* **1994**, *49*, 14251−14269.

(69) Kresse, G.; Joubert, D. From ultrasoft pseudopotentials to the projector augmented-wave method. *Phys. Rev. B:Condens. Matter Mater. Phys.* **1999**, *59*, 1758−1775.

(70) Wellendorff, J.; Lundgaard, K. T.; Møgelhøj, A.; Petzold, V.; Landis, D. D.; Nørskov, J. K.; Bligaard, T.; Jacobsen, K. W. Density functionals for surface science: Exchange-correlation model development with Bayesian error estimation. *Phys. Rev. B:Condens. Matter Mater. Phys.* **2012**, *85*, 235149.

(71) Blöchl, P. E. Projector augmented-wave method. *Phys. Rev. B:Condens. Matter Mater. Phys.* **1994**, *50*, 17953−17979.

(72) Musaelian, A.; Batzner, S.; Johansson, A.; Sun, L.; Owen, C. J.; Kornbluth, M.; Kozinsky, B. Learning local equivariant representations for large-scale atomistic dynamics. *Nat. Commun.* **2023**, *14*, 579.

(73) Perez-Lemus, G.; Xu, Y.; Jin, Y.; Zubieta Rico, P.; de Pablo, J. The importance of sampling the dynamical modes: Reevaluating benchmarks for invariant and equivariant features of machine learning potentials for simulation of free energy landscapes. *J. Chem. Phys.* **2024**, *161*, 244703.

(74) Fu, X.; Wu, Z.; Wang, W.; Xie, T.; Keten, S.; Gomez-Bombarelli, R.; Jaakkola, T. S. Forces are not Enough: Benchmark and Critical Evaluation for Machine Learning Force Fields with Molecular Simulations. In *Transactions on Machine Learning Research*, Survey Certification, 2023.

(75) Han, J.; Zhang, L.; Car, R.; E, W. Deep Potential: A General Representation of a Many-Body Potential Energy Surface. *Commun. Comput. Phys.* **2018**, *23*, 629−639.

(76) Larsen, A. H.; Mortensen, J. J.; Blomqvist, J.; Castelli, I. E.; Christensen, R.; Du lak, M.; Friis, J.; Groves, M. N.; Hammer, B.; Hargus, C. others The atomic simulation environment—a Python library for working with atoms. *J. Phys.: Condens. Matter* **2017**, *29*, 273002.

(77) Zubieta Rico, P. F.; Schneider, L.; Pérez-Lemus, G. R.; Alessandri, R.; Dasetty, S.; Nguyen, T. D.; Menéndez, C. A.; Wu, Y.; Jin, Y.; Xu, Y. others PySAGES: flexible, advanced sampling methods accelerated with GPUs. *npj Comput. Mater.* **2024**, *10*, 35.

(78) Darve, E.; Pohorille, A. Calculating free energies using average force. *J. Chem. Phys.* **2001**, *115*, 9169−9183.

(79) Darve, E.; Rodríguez-Gómez, D.; Pohorille, A. Adaptive biasing force method for scalar and vector free energy calculations. *J. Chem. Phys.* **2008**, *128*, 144120.

(80) Jin, Y.; Perez-Lemus, G. R.; Zubieta Rico, P. F.; de Pablo, J. J. Improving Machine Learned Force Fields for Complex Fluids through Enhanced Sampling: A Liquid Crystal Case Study. *J. Phys. Chem. A* **2024**, *128*, 7257−7268.